




Giant electrophotonic response in two-dimensional halide perovskite $\text{Cs}_3\text{Bi}_2\text{I}_9$ by strain engineering

Srihari M. Kastuar  and Chinedu E. Ekuma *Department of Physics, Lehigh University, Bethlehem, Pennsylvania 18015, USA* (Received 4 August 2022; revised 28 November 2022; accepted 4 January 2023; published 3 February 2023)

Organic-inorganic mixed halide perovskites have been of utmost importance for renewable energy and information technology due to their outstanding properties, but the toxicity of Pb and the instability of the organic component has hindered their applications. Herein, we present detailed mechanical and elastic properties of the family of the Pb-free perovskite-derived two-dimensional (2D) $A_3B_2X_9$ ($A = \text{K, Rb, Cs}$; $B = \text{Bi, Sb, As, P}$; and $X = \text{Cl, Br, I}$), and demonstrate different physical property tunability of the archetypical $\text{Cs}_3\text{Bi}_2\text{I}_9$ using *ab initio* simulations. Our calculated properties show that the optoelectronic properties can be tuned efficiently, as evidenced by flat bands in the band structure and the large absorption peaks in the optical spectra. Through strain engineering, we achieve a redshift of the optical absorption towards the visible regime and demonstrate a robust tuning of the optoelectronic properties for device applications.

DOI: [10.1103/PhysRevMaterials.7.024002](https://doi.org/10.1103/PhysRevMaterials.7.024002)

I. INTRODUCTION

Organic-inorganic mixed halide perovskites have attracted a lot of attention both for fundamental research and practical applications due to their simultaneous superlative energy-efficient properties and low cost. The novel properties are conventionally attributed to long carrier lifetimes, high absorption coefficients, and tunable energy band gaps [1–3]. However, fundamental drawbacks such as the toxicity of Pb, instability of the organic component, and electric field-induced ionic migration have hindered practical applications [4,5]. One way to tackle these drawbacks is to design all-inorganic, Pb-free perovskite-derived materials such as $A_3B_2X_9$ ($A = \text{K, Rb, Cs}$; $B = \text{Bi, Sb, As, P}$; and $X = \text{Cl, Br, I}$). $\text{Cs}_3\text{Bi}_2\text{I}_9$ (CBI) is an archetypal $A_3B_2X_9$, and recent experiments on the bulk show that it is ecofriendly and more stable in humid air [6,7]. However, the excellent optoelectronic properties, such as high absorptivity in traditional Pb-based optoelectronic materials, are significantly diminished [6–8]. Dimensionality reduction has been shown to significantly improve the properties of materials, and in some cases, induce novel physics peculiar in atomically thin two-dimensional (2D) materials. 2D-based $\text{Cs}_3\text{Bi}_2\text{I}_9$ has been recently synthesized and novel properties, e.g., valleytronics, reported [9,10]. However, essential features such as the mechanical and optoelectronic properties are still not clear or unexplored. Herein, we provide baseline computational data and a detailed physical property analysis of 2D $\text{Cs}_3\text{Bi}_2\text{I}_9$ (2D CBI), including mechanical, optoelectronic, and Raman (R) and infrared (IR) spectroscopy to guide future experimental and computational studies. We demonstrate the unique optical and vibrational features that make 2D-derived $\text{Cs}_3\text{Bi}_2\text{I}_9$ a unique optoelectronic material.

II. METHODS

To explore the physical properties of 2D-based $A_3B_2X_9$, we employed first-principles approaches as implemented in two complementary codes, the Vienna *ab initio* simulation package (VASP) [11] and QUANTUM ESPRESSO (QE) [12,13]. The mechanical properties and structural relaxation are carried out using the Perdew-Burke-Ernzerhof (PBE) exchange-correlation functional [14] and the electronic properties are obtained with the Heyd-Scuseria-Ernzerhof (HSE06) hybrid functional [15], incorporating spin-orbit coupling, self-consistently. We used 33% of the Hartree-Fock mixing parameter, which has been shown to accurately describe the properties of 2D materials [16–18]. The Raman and infrared spectroscopy is calculated with density functional perturbation theory (DFPT) [19]. All calculations, self-consistently, included van der Waals interactions via the DFT-D3 method [20,21] and used a plane-wave energy cutoff of 600 eV with a well-converged k -point grid of $8 \times 8 \times 1$ to sample the Brillouin zone, which ensured that the charge (energy) is converged to within 10^{-3} eV (10^{-7} eV), with the residual stresses and forces less than 0.01 GPa and 10^{-3} eV \AA^{-1} . The values of the elastic constants and phonon frequencies are calculated within the numerical error of ± 0.02 N/m and ± 5 cm^{-1} , respectively [see Supplemental Material (SM) [22] for an error analysis].

Mechanical properties and elastic constants are frequently used to determine the stability of structures in both experimental synthesis and integration into devices. At present, such data are lacking for the family of 2D-based $A_3B_2X_9$. To establish the mechanical stability, we performed first-principles calculations with our recently developed ELASTOOL toolkit [23] using VASP as the calculator. The 2D-based $A_3B_2X_9$ generally exhibit hexagonal symmetry. To this end, we have adopted this symmetry in our elastic constant calculations and, as such, only the knowledge of the two independent elastic constants C_{11} and C_{12} is needed to fully characterize the mechanical

*che218@lehigh.edu

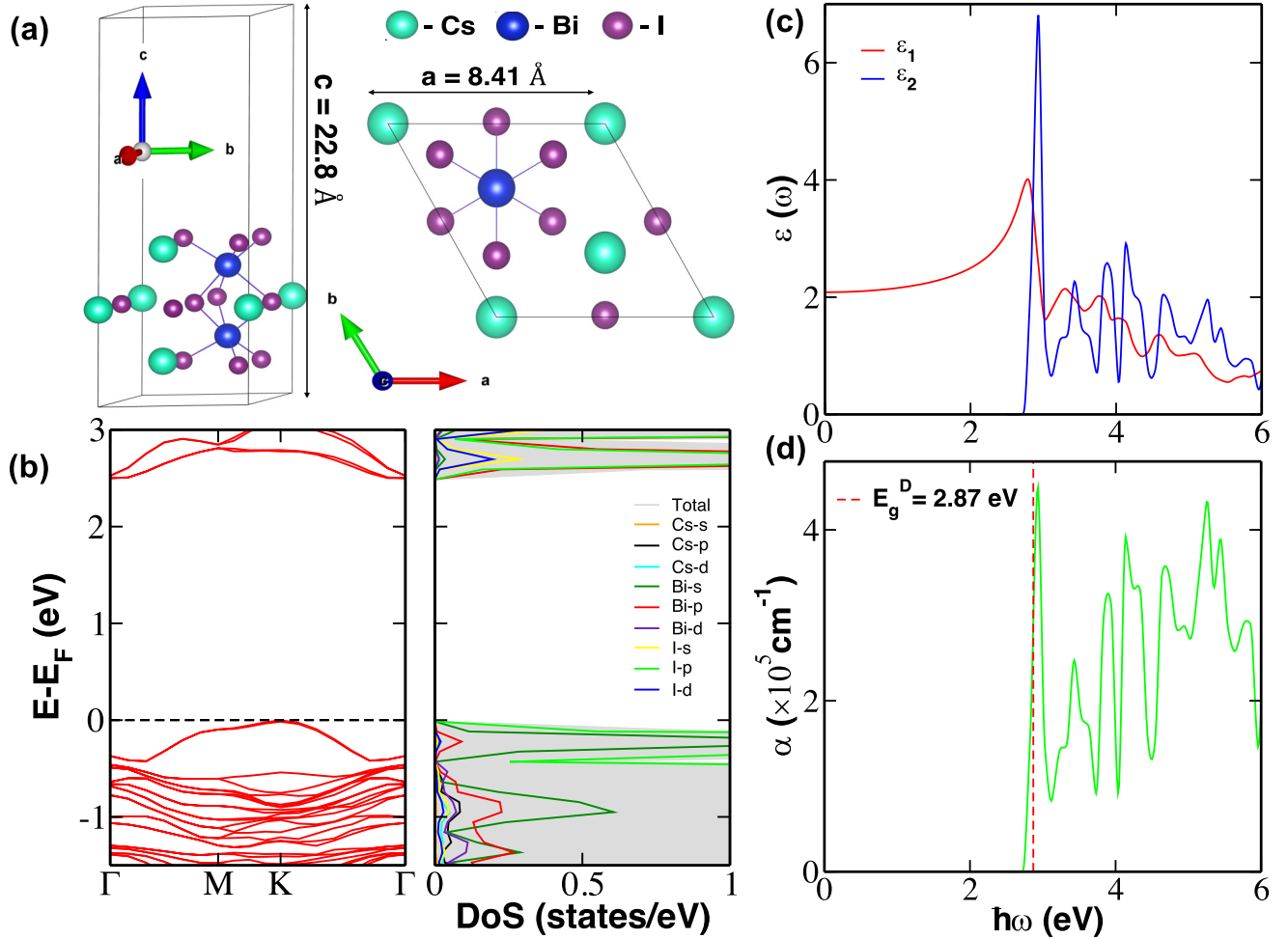


FIG. 1. Structural and HSE06+SOC optoelectronic properties of 2D $\text{Cs}_3\text{Bi}_2\text{I}_9$. (a) The crystal structure, (b) the electronic band structure and the corresponding density and the partial density of states with Fermi energy E_F shifted to zero, (c) the dynamical complex dielectric constant as a function of photon energy, and (d) the optical absorption spectrum as a function of photon energy, showing the onset of absorption at $E_g^o = 2.72$ eV. The red dotted line is the direct energy band gap $E_g^D = 2.87$ eV from our band structure calculation.

properties. Using the computed elastic constants, we obtained the mechanical properties, such as the 2D Young's modulus (Y_{2D}), Poisson ratio (ν), in-plane stiffness constant (K), shear modulus (G), and velocity of sound in both the longitudinal (V_l) and transverse (V_t) directions [24,25] (see Table S1 in the SM [22]). Compared to other 2D materials such as graphene and MoS_2 , 2D-based $\text{A}_3\text{B}_2\text{X}_9$ show relatively smaller mechanical and elastic constant values characterized by very low sound velocities. For example, their average stiffness constant of ~ 8 N/m is orders of magnitude smaller than that of either graphene (~ 340 N/m) or MoS_2 (120 N/m) [26,27], implying very soft material; this could offer a balance between hardness and sustainability, and synthesis, which has been a challenge in applications.

III. RESULTS AND DISCUSSION

Motivated by the recent experimental synthesis of the archetypical $\text{Cs}_3\text{Bi}_2\text{I}_9$ member, we have further explored its properties. In general, 2D CBI exhibits a nontypical YZX_3 perovskite crystal structure [Fig. 1(a)]. A pair of $[\text{BiI}_6]^{-3}$ octahedra share three I atoms forming a $[\text{Bi}_2\text{I}_9]^{-3}$ bioctahedra,

and the Cs atoms occupying the Y-cation positions lead to hexagonal crystal symmetry. A single layer with the $[\text{Bi}_2\text{I}_9]^{-3}$ bioctahedra, three nonidentical Cs atoms (one edge and two within the cell with different z coordinates), and a large vacuum along the c axis forms the unit cell of the monolayer, while the bulk crystal is layered along the c axis with a weak van der Waals interaction between layers. To further confirm the stability, we computed the formation energy per atom, $E_f = (E_{\text{tot}} - \sum_i c_i \mu_i)/N$, where E_{tot} is the total energy of $\text{Cs}_3\text{Bi}_2\text{I}_9$, c_i is the concentration of the different atoms (i), and N is the total number of atoms in the $\text{Cs}_3\text{Bi}_2\text{I}_9$ unit cell. The chemical potential μ_i is approximated with the bulk energy E_i of the constituting elements. The formation energy of the monolayer was found to be -1.93 eV/atom. This implies an exothermic formation process and confirms the energetic stability of the crystal structure. Another important energetic parameter for characterizing a 2D material is the exfoliation energy E_{exf} , which quantifies the amount of energy required to peel a single layer from the surface of a bulk material [28–30]. Herein, we have defined $E_{\text{exf}} = (E_m - E_b)/A$, where E_m (E_b) is the ground state total energy per layer in the unit cell of the monolayer (bulk), and A is the cross-sectional area of

the monolayer unit cell. Our calculated $E_{\text{ext}} \sim 0.22 \text{ J m}^{-2}$ is comparable to the previously reported value of 0.29 J m^{-2} [9], but smaller than the $\sim 0.34\text{--}0.46 \text{ J m}^{-2}$ reported for graphene and hexagonal boron nitride [28,29]. This suggests a small requirement of energy to extract a layer of $\text{Cs}_3\text{Bi}_2\text{I}_9$ from the bulk. Our calculations predict a 2D CBI structure with hexagonal symmetry $P\bar{6}$ and space group No. 174. The predicted symmetry is marginally different from the space group No. 187 with larger $E_f \sim -1.86 \text{ eV/atom}$ previously reported [9] (see Tables S4 and S5 in SM [22]). This presents the possibility of a degenerate ground state of 2D CBI. Such structural behavior has been reported in the bulk counterpart where lower-symmetry phases emerge at lower pressures or temperatures [31].

To gain further insight into the physical properties of 2D CBI, we computed the electronic properties characterized by the electronic band structure and the density of states [Fig. 1(b)] using the HSE06 hybrid functional, including spin-orbit coupling (SOC). We calculated the band structure along the high-symmetry paths $\Gamma(0, 0, 0) - M(1/2, 0, 0) - K(2/3, 1/3, 0) - \Gamma(0, 0, 0)$ in the first Brillouin zone, where the numbers in the parentheses represent the coordinates (u, v, w) of the high-symmetry points in the basis of the reciprocal space primitive translation vectors given by $\vec{b}_1, \vec{b}_2, \vec{b}_3$. The calculated electronic properties with SOC led to an indirect band gap $E^{K-\Gamma} \sim 2.50 \text{ eV}$, which is significantly lower than the $E^{K-\Gamma} \sim 3.08 \text{ eV}$ obtained without SOC. Similarly, spin-orbit coupling has been shown to reduce the band gap of bulk $\text{Cs}_3\text{Bi}_2\text{I}_9$ [32]. Furthermore, the reduction in the band gap due to spin-orbit coupling is commensurate with halide perovskites containing heavy atoms [33–35] and other 2D-based organometallic halide perovskites [36]. We note that the PBE band gap without SOC is closer to the bulk value of $\sim 1.9\text{--}2.2 \text{ eV}$ [32,37]. The states in the proximity of the Fermi level are characterized by flat bands, especially around the valence band edge. The decomposition of the density of states [right panel of Fig. 1(b)] shows that these flat bands are dominated by a strong hybridization between I- p and Bi- s and p states. To quantify the curvature of the band edge states, which describes the transport properties of $\text{Cs}_3\text{Bi}_2\text{I}_9$, we calculated the carrier effective masses m^b by fitting a parabola $E_k = \frac{\hbar^2}{2m_0} \vec{k}^T A \vec{k}$ to the states around the valence (conduction) band maximum (minimum) in the band structure [left panel of Fig. 1(b)], where m_0 is the free-electron mass, $k = (k_x, k_y)$ is the parallel k point measured from the band extremum, and the inverse of the effective masses along the band curvature is given by the eigenvalues of matrix A . The numerical error in this process is $\sim 0.5 \times 10^{-6}$. The calculated electron effective mass m_e^b along k_x (k_y) is 0.95 (0.92) and the corresponding hole effective mass is 0.54 (0.47). This corresponds to an electron and hole Fermi velocity V_F of $\sim 2.60 \times 10^5$ and $1.90 \times 10^5 \text{ m/s}$, respectively. Defining the exciton effective mass μ as $\mu^{-1} = m_e^{-1} + m_h^{-1}$, we obtain $\mu \sim 0.34$ (0.31) along the k_x (k_y) direction. Such values of exciton effective mass could support an exciton condensate and layer-dependent valley polarization [9]. The flat bands in the valence band are intrinsic to the perovskite structure and are independent of crystal dimensionality, as can be seen from the PBE band structures of bulk and few layer flakes $\text{Cs}_3\text{Bi}_2\text{I}_9$ [9,38,39].

The optical spectroscopy, though less direct than the electronic band structure, has the significant advantage of being a true “bulk” probe of the electronic structure of a material. To study the absorption spectra of 2D CBI, we calculated the photon-energy-dependent dielectric function using our HSE06+SOC eigenstates. The imaginary (absorptive) part (ϵ_2) of the complex dielectric function is determined by summing over empty valence and conduction band states, and the real (dispersive) part (ϵ_1) is obtained using the Kramers-Kronig transformation, as implemented in VASP [19]. Thereafter, the frequency-dependent absorption coefficient $\alpha(\omega)$ was obtained as $\alpha(\omega) = \frac{\sqrt{2}\omega}{c} [\sqrt{\epsilon_1^2 + \epsilon_2^2} - \epsilon_1]^{\frac{1}{2}}$, where c is the speed of light in vacuum. The calculated spectra of the complex dielectric function is presented in Fig. 1(c) and the $\alpha(\omega)$ spectrum is shown in Fig. 1(d). The main feature of $\epsilon_1(\omega)$ is the sharp peak structure around 2.78 eV; this is followed by a steep descent with a minimum around 3.02 eV, and subsequently, four smaller peak features around $\sim 3.29\text{--}4.56 \text{ eV}$. After this, the $\epsilon_1(\omega)$ spectra slowly decreased as the curve starts to flatten beyond 6 eV. The absorptive part is characterized by multiple sharp peak features from 2.93 to 4.66 eV, followed by closer small features up to 6 eV. The optical band gap E_g^o is characterized by the direct transition at the same k point and it denotes the onset of absorption at the edge of the absorption spectra. We obtained $E_g^o \sim 2.72 \text{ eV}$, which corresponds to the direct transition along the K point in the band structure, which lies towards the end of the visible region of the electromagnetic spectrum. The direct transitions from the first two almost dispersionless valence bands at the K point correspond to the peak structures at 2.94 and 3.43 eV with large absorption coefficients $\alpha(\omega) \sim 4 \times 10^5$ and $2 \times 10^5 \text{ cm}^{-1}$, respectively [Fig. 1(d)]. We note that our predicted absorption coefficient at the onset of absorption for 2D CBI is more than twice the experimentally observed $\alpha(\omega) \sim 7 \times 10^4 \text{ cm}^{-1}$ at $\sim 2.5\text{--}3.5 \text{ eV}$ for bulk $\text{Cs}_3\text{Bi}_2\text{I}_9$ [40], and comparable to those of organometallic perovskites [41]. Though the HSE06 functional does not fully account for electron-hole interactions, the difference between the direct electronic and optical band gaps can provide some insight into the binding energy. We estimate a binding energy of $\sim 0.15 \text{ eV}$, which is nearly half that reported for bulk Cs-Bi-based halide perovskites that accounted for electron-hole interactions [42]. Due to quantum confinement, we expect the exciton binding energy to be significantly higher in 2D CBI than in the bulk; such calculations require solving the complex Bethe-Salpeter equation, which is beyond the scope of the current research.

Strain engineering is essential for fine tuning the properties of materials. Particularly for the family of 2D-based $A_3B_2X_9$ structures with soft mechanical properties, strain engineering could be used to easily tune their properties [43]. The calculated evolution of the properties of 2D $\text{Cs}_3\text{Bi}_2\text{I}_9$ under both compressional and tensile strain, with and without SOC, are presented in Fig. 2, and Figs. S2– S5 and Table S3 in SM [22]. It is interesting to note that 2D $\text{Cs}_3\text{Bi}_2\text{I}_9$ is more susceptible to compressional than tensile strain due mainly to the larger pressure experienced by the structure under compressional stress (Table S3). We observe that strains of $\sim 10\%\text{--}15\%$ render 2D CBI mechanically unstable, which supports the small elastic

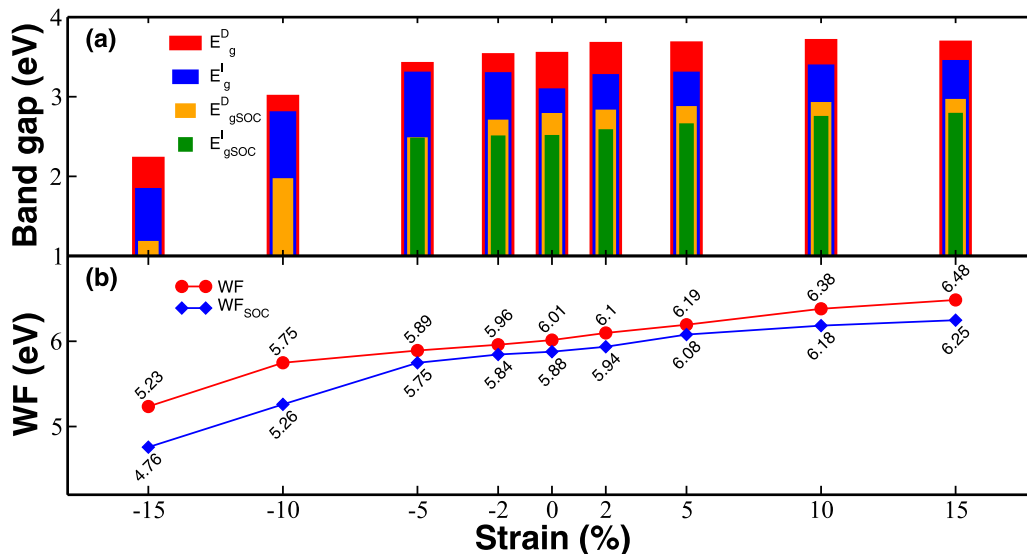


FIG. 2. Strain engineering in 2D Cs₃Bi₂I₉ showing the evolution of (a) the electronic indirect and direct band gap and (b) the work function (WF) as a function of compressional and tensile strains with and without spin-orbit coupling.

and mechanical properties obtained for the pristine structure. We attribute the faster bond-breaking process under strain that led to a decrease in the mechanical properties of 2D CBI to van der Waals dominated interactions within the layer and a reduction of purely directional covalent bonding with the octahedra coordinated atoms that promoted a decrease in the bond energies. To further characterize the modifications of the Cs₃Bi₂I₉ electronic structure under strain, we calculated the energy band gap and the corresponding work function, $\Phi = E_F - E_{\text{vac}}$, where E_{vac} is the reference vacuum energy and E_F is the Fermi level (Fig. 2). We observe that the rate of change of the energy band gap increased as the strain increases. However, under compressional strain, the rate of change of the energy band gap is more pronounced, rendering the direct and indirect energy band gap almost degenerate [Fig. 2(a)]. We also observed that the differences in the band gaps under strain with and without SOC (~ 0.75 eV) are consistent with that seen in the pristine material (~ 0.6 eV). Furthermore, the evolution of the band gap under mechanical strain with and without spin-orbit coupling shows qualitative similarities. Because the work function is a surface property, measuring its variations under different levels of applied strain is useful in predicting the behavior of electronic properties under electron/hole doping in a 2D semiconductor. The impact of applied strain is analogous to how dopant levels in the band gap change the position of the band edges by modifying the work function and vacuum level. Our calculations show that the work function increases (decreases) with increasing tensile (compressional) strain [Fig. 2(b)]. Such a trend is consistent with the evolution of the Fermi level towards the valence band maximum in the electronic band structure (Figs. S2 and S3), and depict the n -doping process in 2D Cs₃Bi₂I₉. The observed high tunability of the electronic properties is also reflected in the optical absorption. The peak structures immediately following the onset of absorption are easily tunable. We observe that compressional strain led to a redshift towards the visible regime, while tensile strain led to a negligible increase in the optical gap (Table S3 and Figs. S4 and S5). Such high

tunability, especially retaining the high absorptivity in the visible regime, suggests that Cs₃Bi₂I₉ could be an important optoelectronic material.

To understand the dynamical changes due to atomic interactions, and further probe the property tunability of 2D Cs₃Bi₂I₉, we compute and explore the phonon and vibrational properties. We characterize the various phonon modes with the Raman (R) and infrared (IR) activities. The most stable crystal structure of 2D CBI belongs to the hexagonal crystal symmetry with point group symmetry C_{3h} (-6). This point group has four real-valued irreducible representations, A' , A'' , E'^* , and E''^* . Using DFPT as implemented in QE, we have calculated the irreducible phonon modes representation at the Brillouin zone center (Γ point): $\Gamma = 7A'(R) + 7A''(I) + 6E''(R) + 6E''^*(R) + 8E'(IR + R) + 8E'^*(IR + R)$. The computed R and IR spectra along with the eigenvectors associated with critical active modes are presented in Fig. 3. The R and IR modes show three distinct peak structures, albeit at different frequencies. The out-of-plane vibrations of these modes establish that they are indeed optical modes (see the eigenvector plots in Fig. 3).

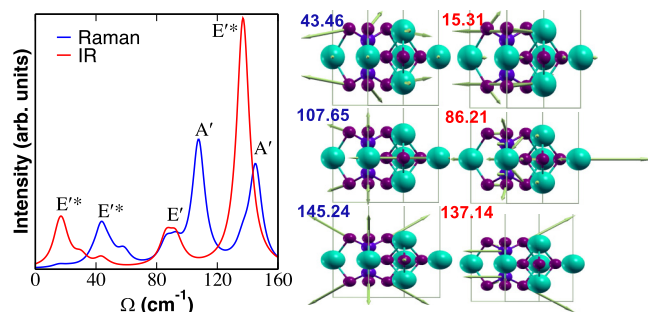


FIG. 3. Calculated Raman and infrared spectra, and the corresponding eigenvectors of the three prominent Raman- (blue) and infrared- (red) active modes with the frequencies in cm⁻¹ of 2D Cs₃Bi₂I₉.

The Raman spectra are characterized by three distinct peak structures. The low-frequency peak structure at 43.46 cm^{-1} is due to the interactions between I and Bi atoms with small vibrations from nonedge Cs atoms and corresponds to the E'^* R-active mode. The A' R-active mode at 107.65 cm^{-1} is highly symmetric with the majority of the contribution coming from identical I (Bi) atoms moving out of phase along the [001] ([010]) direction in the vicinity of almost stationary Cs atoms. We also obtained an R-active A' mode at 145.24 cm^{-1} . Our analysis also shows that this mode is highly symmetric and is dominated by the out-of-phase vibration of Bi atoms along the [001] direction and that of I atoms in the x - z plane, with practically zero contribution from the I atoms bonded to the nonedge relatively stationary Cs atoms. Remarkably, we note that the recent experimental work of Liang and co-workers [9] reported two prominent R-active modes at 109.3 and 145.2 cm^{-1} , in basic agreement with our predicted values. In the IR spectra, we predict an E'^* IR-active mode at 15.31 cm^{-1} . This low-frequency IR-active mode is dominated by the two nonedge Cs atoms. The peak structure at 86.21 cm^{-1} is dominated by I atoms, particularly those bonded to nonedge Cs atoms; this is an E' IR-active mode.

The highest-frequency structure at 137.14 cm^{-1} belongs to the E'^* IR-active mode and its vibrations are entirely from I and Bi atoms of the bioctahedra undergoing symmetric stretching.

In summary, we report detailed results and provide baseline computational data of the structural, electronic, optical, and vibrational properties of 2D CBI, along with the elastic and mechanical properties of 46 CBI-like 2D materials. By quantifying the energetics, we show degeneracy in the structure of 2D CBI within the hexagonal symmetry. With our first-principles calculations, we predict an indirect electronic band gap and large absorption that is visible near the UV region. The optoelectronic features are easily tunable with strain engineering that is robust with high absorptivity in the visible regime.

ACKNOWLEDGMENT

This work is supported by NSF DMR-2202101. S.M.K. acknowledges support from a Lee Graduate Fellowship. Supercomputer support is provided by the CCT@Lehigh.

-
- [1] H. J. Snaith, *Nat. Mater.* **17**, 372 (2018).
- [2] S. D. Stranks, G. E. Eperon, G. Grancini, C. Menelaou, M. J. Alcocer, T. Leijtens, L. M. Herz, A. Petrozza, and H. J. Snaith, *Science* **342**, 341 (2013).
- [3] K. Tanaka, T. Takahashi, T. Ban, T. Kondo, K. Uchida, and N. Miura, *Solid State Commun.* **127**, 619 (2003).
- [4] A. Babayigit, A. Ethirajan, M. Muller, and B. Conings, *Nat. Mater.* **15**, 247 (2016).
- [5] H. Zhu, E.-S. Shin, A. Liu, D. Ji, Y. Xu, and Y.-Y. Noh, *Adv. Funct. Mater.* **30**, 1904588 (2020).
- [6] F. Bai, Y. Hu, Y. Hu, T. Qiu, X. Miao, and S. Zhang, *Sol. Energy Mater. Sol. Cells* **184**, 15 (2018).
- [7] R. Waykar, A. Bhorde, S. Nair, S. Pandharkar, B. Gabhale, R. Aher, S. Rondiya, A. Waghmare, V. Doiphode, A. Punde *et al.*, *J. Phys. Chem. Solids* **146**, 109608 (2020).
- [8] B.-W. Park, B. Philippe, X. Zhang, H. Rensmo, G. Boschloo, and E. M. Johansson, *Adv. Mater.* **27**, 6806 (2015).
- [9] J. Liang, Q. Fang, H. Wang, R. Xu, S. Jia, Y. Guan, Q. Ai, G. Gao, H. Guo, K. Shen *et al.*, *Adv. Mater.* **32**, 2004111 (2020).
- [10] E. E. Morgan, L. Mao, S. M. Teicher, G. Wu, and R. Seshadri, *Inorg. Chem.* **59**, 3387 (2020).
- [11] G. Kresse and J. Furthmüller, *Phys. Rev. B* **54**, 11169 (1996).
- [12] P. Giannozzi, S. Baroni, N. Bonini, M. Calandra, R. Car, C. Cavazzoni, D. Ceresoli, G. L. Chiarotti, M. Cococcioni, I. Dabo, A. Dal Corso, S. de Gironcoli, S. Fabris, G. Fratesi, R. Gebauer, U. Gerstmann, C. Gougoussis, A. Kokalj, M. Lazzeri, L. Martin-Samos *et al.*, *J. Phys.: Condens. Matter* **21**, 395502 (2009).
- [13] P. Giannozzi, O. Andreussi, T. Brumme, O. Bunau, M. B. Nardelli, M. Calandra, R. Car, C. Cavazzoni, D. Ceresoli, M. Cococcioni, N. Colonna, I. Carnimeo, A. D. Corso, S. de Gironcoli, P. Delugas, R. A. Di Stasio, Jr., A. Ferretti, A. Floris, G. Fratesi, G. Fugallo *et al.*, *J. Phys.: Condens. Matter* **29**, 465901 (2017).
- [14] J. P. Perdew, K. Burke, and M. Ernzerhof, *Phys. Rev. Lett.* **77**, 3865 (1996).
- [15] A. V. Krukau, O. A. Vydrov, A. F. Izmaylov, and G. E. Scuseria, *J. Chem. Phys.* **125**, 224106 (2006).
- [16] S. Najmaei, C. E. Ekuma, A. A. Wilson, A. C. Leff, and M. Dubey, *Mater. Today* **39**, 110 (2020).
- [17] J.B. Varley, A. Janotti, and C.G. Van de Walle, *Phys. Rev. B* **81**, 245216 (2010).
- [18] C. Ekuma, *Phys. Rev. B* **99**, 075421 (2019).
- [19] M. Gajdoš, K. Hummer, G. Kresse, J. Furthmüller, and F. Bechstedt, *Phys. Rev. B* **73**, 045112 (2006).
- [20] S. Grimme, J. Antony, S. Ehrlich, and H. Krieg, *J. Chem. Phys.* **132**, 154104 (2010).
- [21] S. Grimme, S. Ehrlich, and L. Goerigk, *J. Comput. Chem.* **32**, 1456 (2011).
- [22] See Supplemental Material at <http://link.aps.org/supplemental/10.1103/PhysRevMaterials.7.024002> for elastic and mechanical properties of 46 CBI-like 2D materials and strain engineering in 2D CBI.
- [23] Z.-L. Liu, C. Ekuma, W.-Q. Li, J.-Q. Yang, and X.-J. Li, *Comput. Phys. Commun.* **270**, 108180 (2022).
- [24] E. Cadelano, P. L. Palla, S. Giordano, and L. Colombo, *Phys. Rev. Lett.* **102**, 235502 (2009).
- [25] A. Politano and G. Chiarello, *Nano Res.* **8**, 1847 (2015).
- [26] Q. Peng and S. De, *Phys. Chem. Chem. Phys.* **15**, 19427 (2013).
- [27] Q. Peng, C. Liang, W. Ji, and S. De, *Phys. Chem. Chem. Phys.* **15**, 2003 (2013).
- [28] J. H. Jung, C.-H. Park, and J. Ihm, *Nano Lett.* **18**, 2759 (2018).
- [29] W. Wang, S. Dai, X. Li, J. Yang, D. J. Srolovitz, and Q. Zheng, *Nat. Commun.* **6**, 7853 (2015).
- [30] T. Björkman, A. Gulans, A. V. Krasheninnikov, and R. M. Nieminen, *Phys. Rev. Lett.* **108**, 235502 (2012).
- [31] V. Machulin, F. Motsnyi, O. Smolanka, G. Svechnikov, and E. Y. Peresh, *Low Temp. Phys.* **30**, 964 (2004).

- [32] B. Ghosh, S. Chakraborty, H. Wei, C. Guet, S. Li, S. Mhaisalkar, and N. Mathews, *J. Phys. Chem. C* **121**, 17062 (2017).
- [33] J. Even, L. Pedesseau, J.-M. Jancu, and C. Katan, *J. Phys. Chem. Lett.* **4**, 2999 (2013).
- [34] D. Wang, B. Wen, Y.-N. Zhu, C.-J. Tong, Z.-K. Tang, and L.-M. Liu, *J. Phys. Chem. Lett.* **8**, 876 (2017).
- [35] J. Even, L. Pedesseau, M.-A. Dupertuis, J.-M. Jancu, and C. Katan, *Phys. Rev. B* **86**, 205301 (2012).
- [36] L. Zhang, X. Zhang, and G. Lu, *J. Phys. Chem. Lett.* **11**, 6982 (2020).
- [37] A. J. Lehner, D. H. Fabini, H. A. Evans, C.-A. Hébert, S. R. Smock, J. Hu, H. Wang, J. W. Zwanziger, M. L. Chabinye, and R. Seshadri, *Chem. Mater.* **27**, 7137 (2015).
- [38] K.-H. Hong, J. Kim, L. Debbichi, H. Kim, and S. H. Im, *J. Phys. Chem. C* **121**, 969 (2017).
- [39] M. Pazoki, M. B. Johansson, H. Zhu, P. Broqvist, T. Edvinsson, G. Boschloo, and E. M. Johansson, *J. Phys. Chem. C* **120**, 29039 (2016).
- [40] M. B. Johansson, H. Zhu, and E. M. Johansson, *J. Phys. Chem. Lett.* **7**, 3467 (2016).
- [41] S. De Wolf, J. Holovsky, S.-J. Moon, P. Loper, B. Niesen, M. Ledinsky, F.-J. Haug, J.-H. Yum, and C. Ballif, *J. Phys. Chem. Lett.* **5**, 1035 (2014).
- [42] S. Rieger, B. J. Bohn, M. Döblinger, A. F. Richter, Y. Tong, K. Wang, P. Müller-Buschbaum, L. Polavarapu, L. Leppert, J. K. Stolarczyk *et al.*, *Phys. Rev. B* **100**, 201404(R) (2019).
- [43] S. Yang, Y. Chen, and C. Jiang, *InfoMat* **3**, 397 (2021).